

Designing an Fe^{III}-Doped Nickel Sulfide/Carbon Nanotube Hybrid Catalyst for Alkaline Electrolyte Membrane Water Electrolyzers and Zn–Air Battery Performances

Pandian Ganesan,* Aleksandar Staykov, Hiroaki Shu, Mitsugu Uejima, and Naotoshi Nakashima*



Cite This: ACS Appl. Energy Mater. 2020, 3, 10961–10975



Read Online

ACCESS |

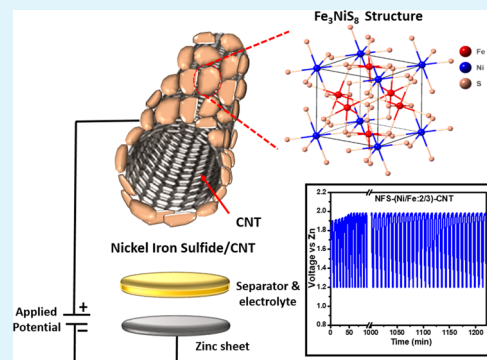
Metrics & More

Article Recommendations

Supporting Information

ABSTRACT: The development of an electrocatalyst with high performance using nonprecious metals/metal oxides as well as its applications in flexible and rechargeable Zn–air batteries and water electrolyzers is in strong demand from industries. In this study, we have designed and synthesized a new $(\text{Fe}_3\text{NiS}_{8-\delta})^{-4+\delta}$ carbon nanotube (CNT) hybrid electrocatalyst and revealed that the catalyst shows a very high oxygen evolution reaction (1.55 V at 10 mA/cm²) and oxygen reduction reaction ($E_{1/2} = 0.82$ V vs RHE) performances. Based on the analyses by *in situ* electrochemical X-ray diffraction together with structure analysis software, *in situ* electrochemical Fourier transform infrared spectroscopy, transmission electron microscopy, and computer simulations, such a high performance is derived from the sulfur vacancies that were formed *via* the self-doped d–p orbitals of Fe^{III} in $(\text{Fe}_3\text{NiS}_{8-\delta})^{-4+\delta}$. Here, we describe an adequate explanation about the role of the iron doping in the nickel sulfides in the catalyst. Furthermore, the fabricated flexible and rechargeable Zn–air and water electrolyzer batteries using the catalyst show a low charge–discharge overpotential gap of 0.66 V and a 237 mA/cm² current density at 1.9 V, which is very important for the development of a rechargeable Zn–air battery and water electrolyzer with a high performance. First-principles calculations are employed to investigate the reaction mechanisms and elucidate the effect of the CNT support for the catalytic activity.

KEYWORDS: alkaline water electrolyzer, Zn–air battery, Fe-doped nickel sulfide, OER, ORR, *in situ* techniques



1. INTRODUCTION

The development of a cost-effective, efficient, and durable bifunctional electrochemical catalyst for the oxygen evolution reaction (OER) and oxygen reduction reaction (ORR) is a key factor for the commercialization of efficient and cost-effective energy conversion and storage devices, such as the zinc–air battery, water electrolyzer, and smart-grid energy storage system.^{1–4} Precious metals, such as Pt and Ir, have been used as the efficient catalysts for the ORR and OER,^{5,6} respectively; however, they are expensive and their deposits on earth are limited, which are the major drawbacks of these metals. For a sustainable and environment-friendly society, the development of a catalyst using cost-effective and earth-abundant metals is highly important. Thus far, various nonprecious metal oxides have been used as catalysts for the OER, ORR, and metal–air batteries.^{7,8} To date, sulfide-doped transition metals and carbon were widely reported for the lithium–sulfur batteries, Zn-ion batteries, and Li-ion battery applications.^{9,10} Transition-metal chalcogenides are some of the promising materials which can compete with the state-of-the-art catalysts in an alkaline medium. These electrochemical tuned (ECT) metal oxides, such as ECT-CoO, ECT-Co_{0.5}Fe_{0.5}O₂, and ECT-Co_{0.37}Ni_{0.26}Fe_{0.37}O₂, showed superior performances compared to their pristine metal oxides.¹¹ However, the durability of their

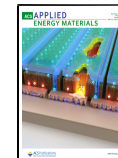
OER and ORR activities was not competitive compared to that of the state-of-the-art catalysts using Pt and IrO₂.^{12,13} The lack of durability has been due to the phase transformation of the metal chalcogens to metal oxides during the electrochemical reactions of the fuel cells, water electrolyzers, and metal–air batteries.^{11–17} Metal sulfides containing chalcogenides have been reported to show a high activity that competes with the precious metal catalysts that have been used in the commercial market.^{12,13} Even now, a clear understanding from both the theoretical and experimental points of view for the metal sulfide phase changes with the applied potential using the so-called Pourbaix diagram has not yet been reported.^{1,11,14,15,18–20}

The use of carbon supports for various nonprecious catalysts, such as CoNiFe–S MNs, Zn–Co–sulfides, LaNiO₃/carbon nanotubes (CNTs), Co_{1-x}S/NS-GN,

Received: August 11, 2020

Accepted: October 27, 2020

Published: November 9, 2020



$\text{Fe}_{0.1}\text{Ni}_{0.9}\text{Co}_2\text{O}_4$, $\text{N},\text{S}-\text{Co}_9\text{S}_8$, and so forth, enhances the rechargeable zinc–air battery performance.^{2–4,21–27} Iron-incorporated transition-metal catalysts, such as FeCo-N , $\text{NiFe}(\text{oxy})$ hydroxides, and iron–nickel sulfides, have been reported to show good zinc–air battery and OER performances compared to those without iron incorporation.^{28–31} The sulfur-doped carbon supports are reported to be good supports for the metal sulfides for ORR and OER.^{12,13,21,46} The oxidation state of iron in these catalysts is +3. In the case of the NiFe (oxy) hydroxides derived from NiFe disulfides before activating to oxy hydroxides, Fe was reported to be in the +2 oxidation state, and after the activating process, it changed to the active form of the +3-oxidation state.³¹ The general explanation of this unusual valence state of Fe^{III} was reported by Khomskii *et al.*³² The Fe^{III} valence state and this behavior suggested that the catalyst is in between the sulfides and persulfides.^{32–34} The use of *in situ* electrochemical spectroscopies and X-ray diffraction (XRD) are expected to be powerful tools to reveal and understand such a unique electronic state behavior.³⁵

It is highly important to shed light on the generation of the Fe^{III} state in a catalyst with a very high electrochemical performance as well as to reveal its detailed mechanism because such a study will provide a hint to develop promising next-generation cost-effective catalysts with a high electrochemical performance. Figure 1 shows the concept of our

copy (HR-TEM), high-angle annular dark field-scanning TEM (HAADF-STEM), STEM imaging, *in situ* electrochemical XRD, Fourier transformed infrared (FT-IR) spectroscopy, X-ray photoelectron spectroscopy (XPS), and an electrochemical method to evaluate their Zn–air battery and water electrolyzer performances. We also conducted a density functional theory (DFT) study in order to determine the mechanism of the catalyst reactions. Based on such analyses, we revealed that our catalyst has a superior ORR, OER, and Zn–air performance compared to the conventional state-of-the-art catalysts in which the formation of Fe^{III} plays an important role.

As a carbon support, we used CNTs because they have a good electrical conductivity and high electrochemical stability because of their high degree of graphitization.^{36–38} In this study, we synthesized three different CNT-hybridized S-doped Ni/Fe catalysts denoted as NFS-(Ni/Fe:1/4)-CNT, NFS-(Ni/Fe:2/3)-CNT, and NFS-(Ni/Fe:3/2)-CNT by changing the composition ratios of the Fe and Ni ions. For comparison, we synthesized S-doped Ni (denoted as NS-CNT) and S-doped Fe catalysts (denoted as FS-CNT) as well as NFS-(Ni/Fe:2/3) not containing CNTs (for details, see the Supporting Information, Section S1.1). The compositions of these catalysts are listed in Table 1. In this study, we focus on (i) the formation of Fe^{III} in Fe_3NiS_8 prepared by the hybridization with CNTs, (ii) the role of the Fe^{III} -rich 020 and 200 crystal planes in enhancing the discharging (ORR) and charging (OER) performance of the fabricated Zn–air battery and water electrolyzer, and (iii) the relation between these unusual behaviors of iron incorporation into the nickel sulfides based on the electrode kinetics. We used supergrowth single-walled CNTs(SWCNTs) as the carbon support because they have a high surface area of $>800 \text{ m}^2/\text{g}$, which is expected to lead to a high electrochemical performance.

2. RESULTS AND DISCUSSION

We synthesized six catalysts by using the conventional solvothermal method (for details, see the Supporting Information, Section S1.1), in which the nickel–iron sulfides were synthesized by decomposing nickel and iron thiourea complexes with specific composition ratios along with the CNTs (see Table 1).

2.1. Structural and Morphological Characterizations.

As will be described later, NFS-(Ni/Fe:2/3)-CNT was characterized with the highest electrochemical performance. In Figure 2, the XRD diagrams of NFS-(Ni/Fe:2/3)-CNT and NFS-(Ni/Fe:2/3) and their simulated patterns are shown. The detailed deduction of the XRD simulations for NFS-(Ni/Fe:2/3)-CNT and NFS-(Ni/Fe:2/3) are shown in the Supporting Information, Section S2.³⁹ We used CrystalMaker (software) and calculated their structures. Figure 2 shows the XRD diagrams of NFS-(Ni/Fe:2/3)-CNT (Figure 2a,c) and NFS-

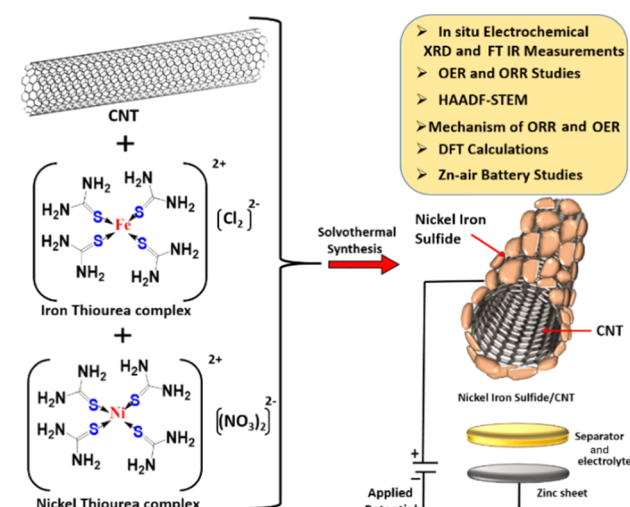


Figure 1. Schematic representation of the aim and scope of this study.

study, in which we design and synthesize CNT-hybridized S-doped Fe/Ni catalysts. The synthesis was carried out by a simple solvothermal method, and the obtained catalysts were characterized by high-resolution transmission electron micros-

Table 1. Composition Ratios of the Catalysts^a

Ni(TU) ₄ (NO ₃) ₂ /mg	Fe(TU) ₄ Cl ₂ /mg	SWCNTs/mg	catalyst abbreviation
20	80	60	NFS-(Ni/Fe:1/4)-CNT
40	60	60	NFS-(Ni/Fe:2/3)-CNT
60	40	60	NFS-(Ni/Fe:3/2)-CNT
40	60	0	NFS-(Ni/Fe:2/3)
100	nil	60	NS-CNT
nil	100	60	FS-CNT

^aTU = thiourea.

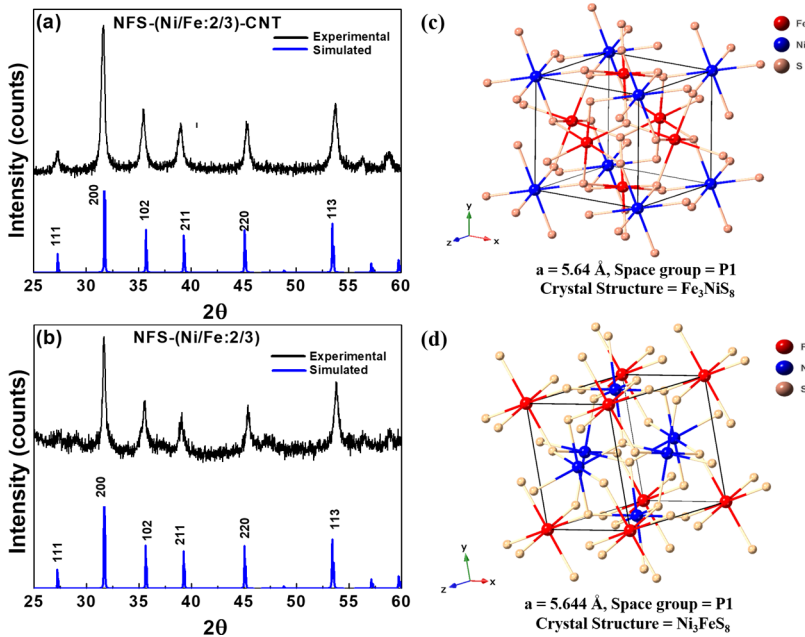


Figure 2. XRD diagrams of (a) NFS-(Ni/Fe:2/3)-CNT and (b) NFS-(Ni/Fe:2/3) and their well-fitted crystal structures, (c) NFS-(Ni/Fe:2/3)-CNT, and (d) NFS-(Ni/Fe:2/3) based on the simulation using CrystalMaker (software).

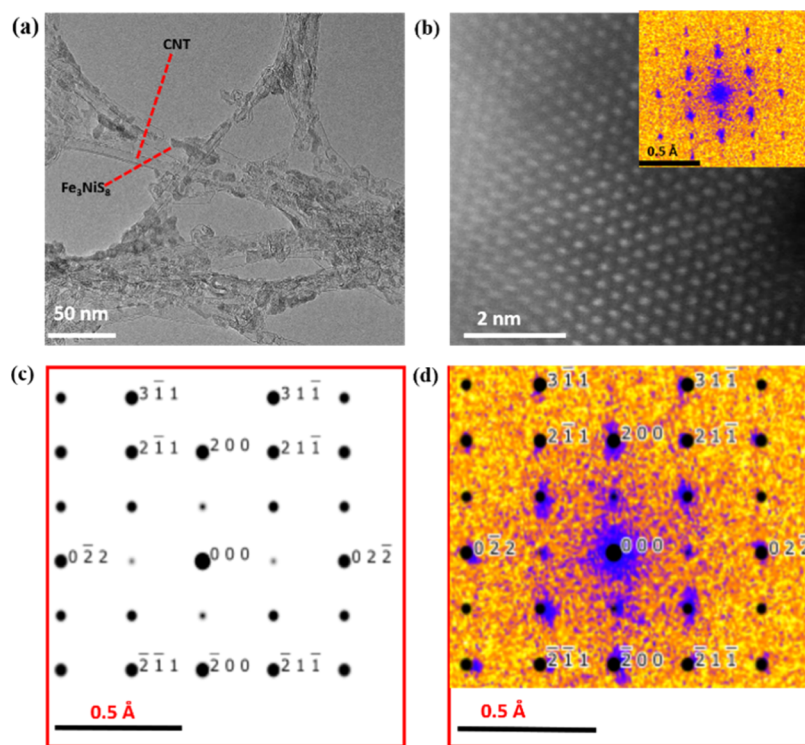


Figure 3. (a) TEM image of NFS-(Ni/Fe:2/3)-2/3. (b) Atomic-resolution TEM images and the (inset) corresponding FFT of NFS-(Ni/Fe:2/3)-2/3. (c) Computed FFT pattern and indexed for Fe_3NiS_8 of NFS-(Ni/Fe:2/3)-2/3 from the CIF. (d) Overlay of FFT from atomic-resolution STEM and the simulated Fe_3NiS_8 XRD pattern (Figure 2a).

(Ni/Fe:2/3) (Figure 2b,d). We used CrystalMaker to fit these structures and found that the Fe_3NiS_8 crystal structure fits well with the data of NFS-(Ni/Fe:2/3)-CNT (Figure 2a,c), and the Ni_3FeS_8 crystal structure fits well with that of NFS-(Ni/Fe:2/3) (Figure 2b,d). The Cartesian coordinates used for the Fe_3NiS_8 and Ni_3FeS_8 structures are provided in Tables S1 and S2, respectively, in which the Fe_3NiS_8 and Ni_3FeS_8 structures were both found to have the $P1$ space group (Figure 2c,d).

The lattice parameter of the simulated Fe_3NiS_8 structure of NFS-(Ni/Fe:2/3)-CNT was 5.640 \AA (Figure 2c), and the α , β , and γ values of the Fe_3NiS_8 structure were 90° . The Ni_3FeS_8 structure in NFS-(Ni/Fe:2/3) exhibited a lattice parameter a of 5.644 \AA (Figure 2d), and the α , β , and γ values of Fe_3NiS_8 were 90° . In the Fe_3NiS_8 structure of NFS-(Ni/Fe:2/3)-CNT, the Fe atoms occupied the face-centered lattice of the unit cell, and the corner of the unit cell was occupied by the Ni atom

(Figure 2b), while in the case of Ni_3FeS_8 in NFS-(Ni/Fe:2/3), the Ni atoms occupied the face-centered lattice of the unit cell, and the corner of the unit cell was occupied by the Fe atoms. Fe_3NiS_8 of NFS-(Ni/Fe:2/3)-CNT exhibits peaks at 27.59° , 31.82° , 35.77° , 39.27° , 45.69° , and 54.16° , which were attributed to the 111, 200, 102, 211, 220, and 113 planes, respectively (Figure 2a).

In Ni_3FeS_8 of NFS-(Ni/Fe:2/3), we observed peaks at 27.44° , 31.58° , 35.55° , 39.10° , 45.52° , and 54.06° , which were attributed to the 111, 200, 102, 211, 220, and 113 planes, respectively (Figure 2b). The 220 and 113 planes were also referred to as the 022 and 311 planes, respectively, because of the lattice parameter similarity. NFS-(Ni/Fe:2/3)-CNT and NFS-(Ni/Fe:2/3) show XRD patterns which are in between the NiS_2 and FeS_2 XRD patterns (Figure S1), while NFS-(Ni/Fe:2/3)-CNT and NFS-(Ni/Fe:2/3) exhibited a Fe_3NiS_8 structure and a Ni_3FeS_8 structure, respectively. Unlike NFS-(Ni/Fe:2/3)-CNT and NFS-(Ni/Fe:2/3), NS-CNT has a NiS_2 structure (ICDD no. 00-002-0850) (Figure S2). Figure 3 shows the TEM images of NFS-(Ni/Fe:2/3)-CNT, in which we clearly observe nanoclusters, which indicated that the catalyst nanoparticles with the size of 10–17 nm are well deposited on the CNT tubes.

To further verify the simulated Fe_3NiS_8 crystal structure of NFS-(Ni/Fe:2/3)-CNT, we have displayed the fast Fourier transform (FFT) from the atomic-resolution STEM image (Figure 3b inset) and also computed the FFT pattern (Figure 3c) for Fe_3NiS_8 of NFS-(Ni/Fe:2/3)-2/3 using its crystallographic information file (CIF) and single-crystal software (the FFT was aligned in the 110 plane and a camera lens width of 44.4 cm). The overlay of FFT from the simulated XRD pattern of Fe_3NiS_8 (black dots with miller indices in Figure 3d) and STEM images (blue dots in Figure 3d) superimposes precisely, which further confirms the formation of the Fe_3NiS_8 crystal structure in NFS-(Ni/Fe:2/3)-CNT. In order to understand the crystal arrangements of NFS-(Ni/Fe:2/3)-CNT, the atomic pattern using the high-angle annular dark-field (HAADF) images of NFS-(Ni/Fe:2/3)-CNT was obtained, and the data are shown in Figure 4a. In addition, by using CrystalMaker software, the crystal arrangement module of the Fe_3NiS_8 structure based on the HAADF images and XRD (Figure 2a,b) of NFS-(Ni/Fe:2/3)-CNT is shown in Figure 4b. As can be seen in Figure 4a,b, the distance between any two planes in the atomic pattern of NFS-(Ni/Fe:2/3)-CNT is 2.82 nm, which precisely agrees with the d_{200} plane of the Fe_3NiS_8 structure that is seen in the XRD pattern of NFS-(Ni/Fe:2/3)-CNT (see Figure 2a). In the HAADF pattern (Figure 4a), some of the sulfur sites are revealed to be vacant in the crystal arrangement, whose crystal arrangement by Crystal-Maker (software) is depicted in Figure 4b. Such vacancies play important roles for the higher ORR and OER activities by tuning the electrochemical surface properties of the metal chalcogens during the electrochemical reactions.^{40–44} The STEM elemental mapping of NFS-(Ni/Fe:2/3)-CNT is shown in Figure 5, in which sulfur (Figure 5b), nickel (Figure 5d), iron (Figure 5c), and carbon (Figure 5e) are almost homogeneously distributed on the tubes. This result indicated that the amount of iron is much higher than that of nickel, which agreed with the iron and nickel structural composition in the XRD (Figure 2).

2.2. XPS Analysis. The XPS spectra of NFS-(Ni/Fe:2/3)-CNT, NFS-(Ni/Fe:2/3), NS-CNT, and FS-CNT are shown in Figure 6. Their S 2p binding energies were found to appear

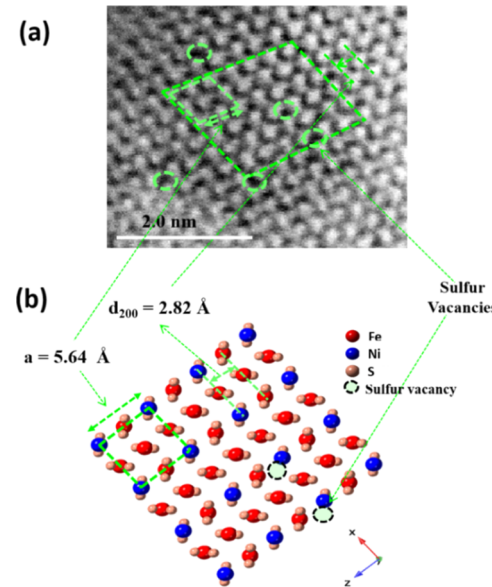


Figure 4. (a) HAADF-STEM dark-field image of NFS-(Ni/Fe:2/3)-2/3 explaining the fringe width, unit cell arrangement, lattice constant value, and sulfur vacancies. (b) Crystal arrangement module 3D structure of Fe_3NiS_8 from the simulated structure using CrystalMaker software explaining the fringe width, unit cell arrangement, lattice constant value, and sulfur vacancies.

at somewhat different energy levels, as shown in Figure 6a. The peaks of NFS-(Ni/Fe:2/3)-CNT that appeared at 162.55 and 163.8 eV are the characteristic peaks observed in iron disulfides and nickel disulfides (S^{2-}),^{40–42,45} and the peak at ~ 165.1 eV is the characteristic peak of sulfur-doped carbon (C–S–C).⁴⁶ NFS-(Ni/Fe:2/3) also exhibited S 2p peaks at 162.7 and 163.7 eV like NFS-(Ni/Fe:2/3)-CNT. Unlike NFS-(Ni/Fe:2/3)-CNT and NFS-(Ni/Fe:2/3), the S^{2-} binding energy of NS-CNT appeared at 162.01 and 164.02 eV. Thus, iron in NFS-(Ni/Fe:2/3)-CNT and NFS-(Ni/Fe:2/3) exhibited iron doping. The peak appeared at 169.25 eV, suggesting nickel–iron incorporation.⁴⁶ The Ni 2p spectra of NFS-(Ni/Fe:2/3)-CNT, NS-CNT, and NFS-(Ni/Fe:2/3) are shown in Figure 6b, in which NFS-(Ni/Fe:2/3)-CNT shows peaks at around 856 and 854 eV, which correspond to Ni of the +2 and +3 oxidation states, respectively. This result indicated that Ni is in the mixed oxidation state,^{31,32} which suggested the formation of sulfur atom bridging (Ni–S–Fe) between Ni and Fe.^{47–49} Based on these results, it is suggested that there are two oxidation states, Ni^{III} and Ni^{II} , in NFS-(Ni/Fe:2/3)-CNT derived from two different bondings between the Fe atoms and the sulfur atoms, namely, $\text{Ni}^{\text{II}}-\text{S}-\text{Fe}^{\text{III}}$ and $\text{Ni}^{\text{III}}-\text{S}-\text{Fe}^{\text{III}}$. NFS-(Ni/Fe:2/3) exhibited a very broad peak top appearing at 854 eV, which suggested the formation of only the Ni^{II} oxidation state in this catalyst. Unlike NFS-(Ni/Fe:2/3)-CNT, the XRD of NS-CNT is not clear; meanwhile, we see a weak peak at ~ 855 eV, which implies the existence of only the +2-oxidation state of Ni.^{31,32} The C 1s spectra of the CNTs, NFS-(Ni/Fe:2/3)-CNT, and NS-CNT are shown in Figure 6c, in which the CNTs and NS-CNT exhibited the characteristic sp^2 carbon binding energy at 284.6 eV,^{2,50} while for NFS-(Ni/Fe:2/3)-CNT, it appeared at 285.5 eV,² which shifted to a higher energy level by 0.9 eV compared to the CNTs. Such a shift suggested an electronic interaction between the CNTs and nickel–iron–sulfide catalyst.

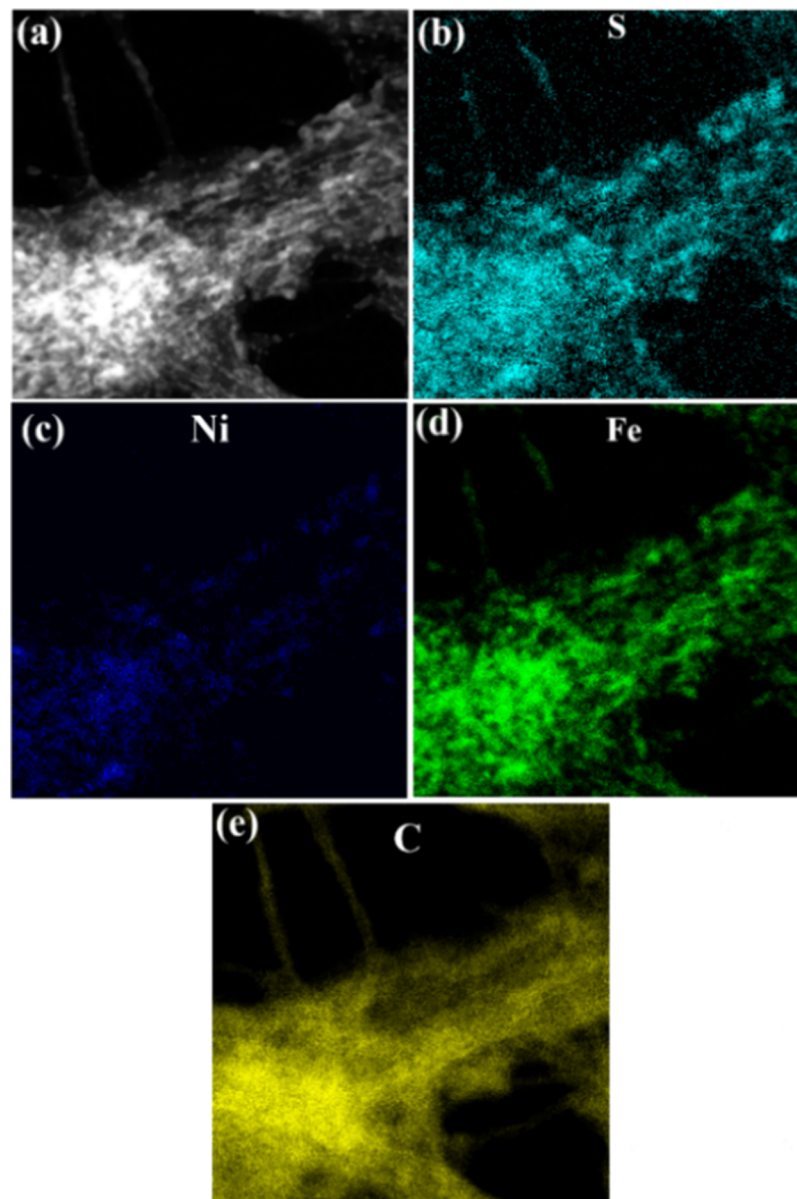


Figure 5. (a) STEM bright-field image of NFS-(Ni/Fe:2/3)-CNT. (b–e) Elemental mapping of sulfur, nickel, iron, and carbon, respectively.

Interestingly, for NFS-(Ni/Fe:2/3)-CNT, new binding energies are clearly observed at 289.3 (weak), 290.5, and \sim 291.5 (shoulder) eV, which would be derived from the C–S, C=S, and S=C=S bonding, respectively, indicating the presence of sulfur doping with the CNTs in NFS-(Ni/Fe:2/3)-CNT.^{2,50} NS-CNT does not exhibit the C–S–C characteristic XPS binding energy, whereas for NFS-(Ni/Fe:2/3)-CNT, we observed the C–S–C binding energy at 165.07 eV (Figure 6c), which indicated the sulfur doping in NFS-(Ni/Fe:2/3)-CNT.^{43,44,46} The Fe 2p XPS spectra of NFS-(Ni/Fe:2/3)-CNT, NFS-(Ni/Fe:2/3), and FS-CNT are shown in Figure 6d, in which NFS-(Ni/Fe:2/3)-CNT exhibits the characteristic binding energies of Fe in the +3-oxidation state at 711.9 and 725.3 eV.^{51,52} FS-CNT provided binding energies at 713.4 and 727.1 eV, suggesting the existence of Fe in the +3 oxidation state.^{51,52} The observed binding energy shift in the positive direction by 1.5 and 1.84 eV compared to those of NFS-(Ni/Fe:2/3)-CNT would be due to the bridging nature of the Ni–S–Fe bonding.^{53,54} The 1.5 eV shift in the Fe³⁺

binding energy of NFS-(Ni/Fe:2/3)-CNT is not due to the Fe⁰ state or Fe²⁺ state. The greater binding energy would be derived from the stronger bonding^{53,54} derived from the bridging S atoms in NFS-(Ni/Fe:2/3)-CNT. In contrast, the peak of the Fe^{III} binding energy of NFS-(Ni/Fe:2/3) is much weaker than those of NFS-(Ni/Fe:2/3)-CNT and FS-CNT, indicating that Fe in NFS-(Ni/Fe:2/3) is mostly in the Fe^{II} state. Further, we calculated the iron-to-nickel ratio as follows: based on the XRD structure (Figure 2), the ratios of Fe/Ni in NFS-(Ni/Fe:2/3)-CNT and NFS-(Ni/Fe:2/3) are 3:1 and 1:2.7, respectively. The obtained results indicate that the CNTs play an important role in the formation of the Fe^{III} oxidation state in the catalyst, that is, the existence of electron transfer between the CNTs and nickel–iron sulfides in NFS-(Ni/Fe:2/3)-CNT is strongly suggested. Figure 6e shows a suggested bonding structure of NFS-(Ni/Fe:2/3)-CNT obtained by the CrystalMaker software. The bond lengths between Ni^{II}–S in NiS₂ and Fe^{II}–S in FeS₂ obtained by CrystalMaker are \sim 2.362 and 2.254 Å, respectively, while the

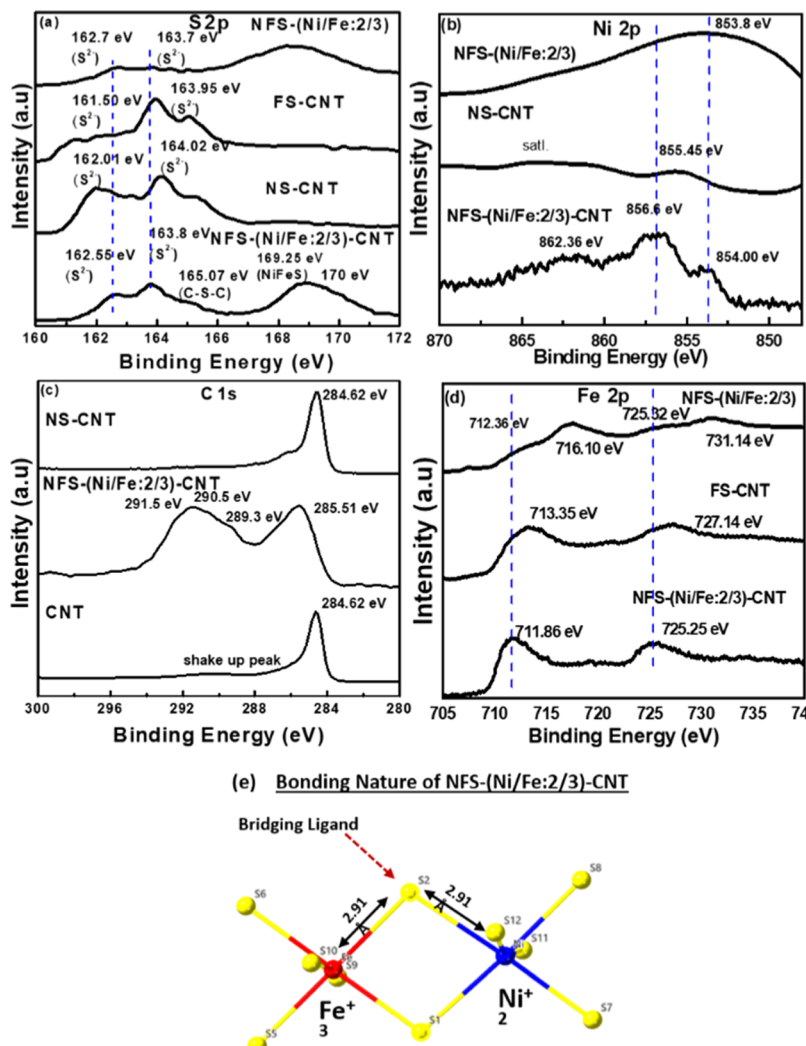


Figure 6. (a) S 2p XPS spectra of NFS-(Ni/Fe:2/3)-CNT, NFS-(Ni/Fe:2/3), NS-CNT, and FS-CNT. (b) Ni 2p XPS spectra of NFS-(Ni/Fe:2/3)-CNT, NFS-(Ni/Fe:2/3), and NS-CNT. (c) C 1s spectra of the SWCNT, NFS-(Ni/Fe:2/3)-CNT, and NS-CNT. (d) Fe 2p XPS spectra of NFS-(Ni/Fe:2/3)-CNT, NFS-(Ni/Fe:2/3), and FS-CNT. (e) Possible structure of NFS-(Ni/Fe:2/3)-CNT visualizing its bonding nature.

bond length between the Ni–S and $\text{Fe}^{\text{III}}\text{–S}$ bonds in the Fe_3NiS_8 structure is 2.391 Å. As can be seen in Figure 6e, both bond lengths of $\text{Fe}^{\text{III}}\text{–S}$ and $\text{Ni}^{\text{II}}\text{–S}$ are 2.91 Å, which is significantly elongated compared to those of the $\text{Fe}^{\text{II}}\text{–S–Ni}^{\text{II}}$ bonding. Furthermore, based on the oxidation states of nickel, iron, and sulfides, we have made conclusions that the charge borne by the crystal structure of NFS-(Ni/Fe:2/3)-CNT is $(\text{Fe}_3\text{Ni}_{8-\delta})^{-4+\delta}$. In order to maintain the charge neutrality in the $(\text{Fe}_3\text{Ni}_{8-\delta})^{-4+\delta}$ structure, there are a lot of sulfur vacancies in the crystal structure of NFS-(Ni/Fe:2/3)-CNT (HAADF image, Figure 4a). This is one of the important parameters responsible for the greater number of sulfur vacancies in the crystal structure of $(\text{Fe}_3\text{Ni}_{8-\delta})^{-4+\delta}$.

2.3. Electrochemical Performance Using Three Electrode Studies. The ORR and OER performance measurements of the synthesized catalysts were carried out in 0.1 M KOH alkaline aqueous solutions at 1600 rpm, as described in Section S1.2 in the Supporting Information, and the results are shown in Figures 7a,b and S3. The observed ORR half-wave potential ($E_{1/2}$) of NFS-(Ni/Fe:2/3)-CNT was 0.81 V, indicating that its activity is better than those of NS-CNT ($E_{1/2} = 0.79$ V) and FS-CNT ($E_{1/2} = 0.80$ V) (Figure 7a), and the $E_{1/2}$ of NFS-(Ni/Fe:2/3) is also 0.80 V. The ORR $E_{1/2}$

potentials of NFS-(Ni/Fe:2/3)-CNT (0.81 V) and Pt/C (Figure 7a) (0.81 V) are the same, implying that the ORR activity of NFS-(Ni/Fe:2/3)-CNT is superior. The ORR accelerated durability test of NFS-(Ni/Fe:2/3)-CNT was carried out using linear sweep voltammetry at 1600 rpm under O_2 -saturated conditions, and the result is shown in Figure S3c. It was revealed that even after 10,000 cycles, the $E_{1/2}$ of the catalyst is almost similar to the initial $E_{1/2}$, and even after 20,000 cycles, a small negative shift of $E_{1/2}$ was observed. It is obvious that the ORR durability is very high.

On the other hand, although NFS-(Ni/Fe:2/3) exhibited a good ORR $E_{1/2}$, its durability is very low, as shown in the continuous cyclic voltammetric sweeping in Figure S3d. Hence, CNT-supported nickel–iron sulfide with the Fe^{III} oxidation state exhibited a good ORR activity and stability. The ORR $E_{1/2}$ values of NFS-(Ni/Fe:1/4)-CNT and NFS-(Ni/Fe:3/2)-CNT are 0.63 and 0.69 V, respectively (Figure S3a), indicating that their ORR activity is much lower than that of NFS-(Ni/Fe:2/3)-CNT. The results clearly revealed that the Ni/Fe composition ratio is highly important for obtaining a high ORR activity. For OER, as shown in Figure 7b, NFS-(Ni/Fe:2/3)-CNT shows that the potential at 10 mA/cm² (benchmark) is 1.55 V versus RHE, which is superior

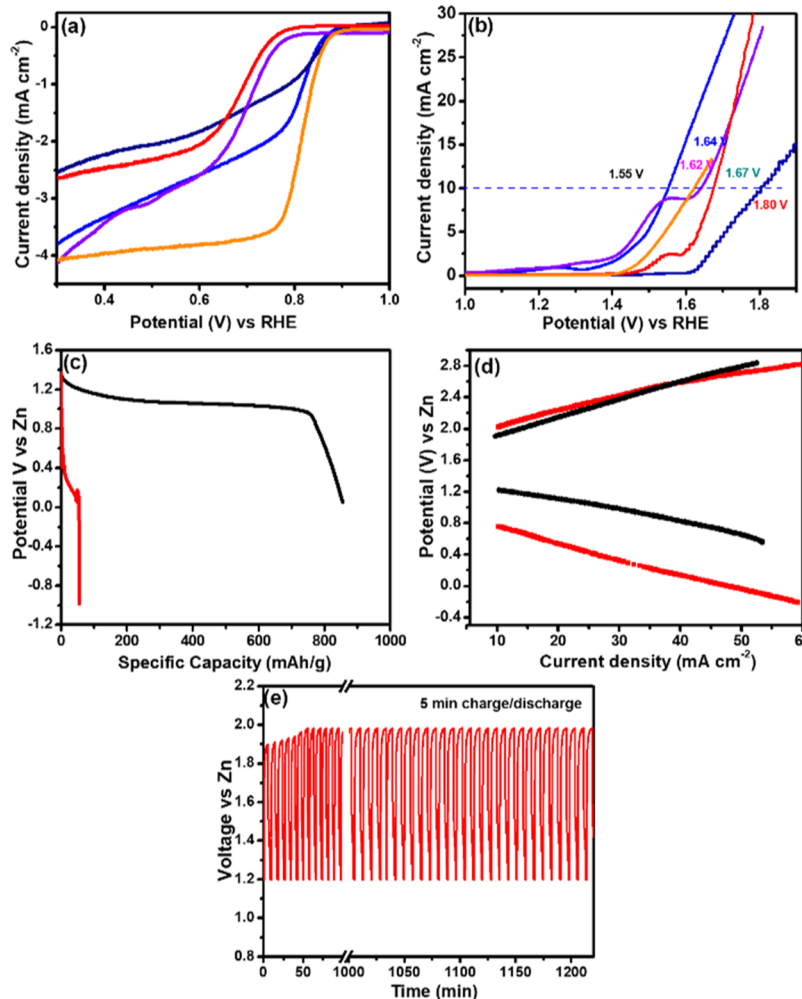


Figure 7. (a) ORR activity of NFS-(Ni/Fe:2/3)-CNT (blue color), NFS-(Ni/Fe:2/3) (navy-blue color), FS-CNT (violet color), NS-CNT (red color), and Pt/C (orange color) using a rotating disk electrode (RDE) at 1600 rpm. (b) OER activity of NFS-(Ni/Fe:2/3)-CNT (blue color), NFS-(Ni/Fe:2/3) (navy-blue color), FS-CNT (violet color), NS-CNT (red color), and Pt/C (orange color) using the RDE at 1600 rpm. (c) Deep-discharge studies of NFS-(Ni/Fe:2/3)-CNT (black color) and NFS-(Ni/Fe:2/3) (red color). (d) I – V curves of the zinc–air batteries using NFS-(Ni/Fe:2/3)-CNT (black color) and NFS-(Ni/Fe:2/3) (red color). (e) Charge/discharge durability of the Zn–air battery using NFS-(Ni/Fe:2/3)-CNT.

Table 2. Comparison of Oxidation States, Crystal Structures, and OER and ORR Activities of the Synthesized Catalysts

catalyst	NFS-(Ni/Fe:2/3)-CNT	NFS-(Ni/Fe:2/3)	NS-CNT	FS-CNT
Ni oxidation state	+2, +3	+2	+2	nil
Fe oxidation state	+3	+2, +3	nil	+3
crystal structure	(Fe ₃ NiS _{8-δ}) ^{-4+δ}	(Ni ₃ FeS _{8-δ}) ^{-8+δ}	NiS ₂	(Fe ₉ S ₁₀ , Fe ₃ S ₄)
$E_{1/2}$ of ORR (V)	0.81	0.80	0.79	0.80
OER potential (E_{OER}) at 10 mA/cm ² (V)	1.55	1.80	1.67	1.64
oxygen electrode potential $ΔE = (E_{1/2} - E_{\text{OER}})$	0.74	1	0.88	0.84

to those of FS-CNT ($E_{10\text{mA/cm}^2} = 1.64$ V), NFS-(Ni/Fe:2/3) ($E_{10\text{mA/cm}^2} = 1.80$ V), and NS-CNT ($E_{10\text{mA/cm}^2} = 1.67$ V). Notably, the OER activity of NFS-(Ni/Fe:2/3)-CNT is higher than that of a conventional RuO₂ catalyst ($E_{10\text{mA/cm}^2} = 1.80$ V). We examined the effect of Ni/Fe composition ratios on the catalysts, and the result is shown in Figure S3b, in which the OER activity of NFS-(Ni/Fe:3/2)-CNT is almost the same as that of NFS-(Ni/Fe:2/3)-CNT, while the activity of NFS-(Ni/Fe:1/4)-CNT ($E_{10\text{mA/cm}^2} = 1.55$ V) is much lower than those of the other two catalysts. Such an activity difference would be due to the difference in the catalyst crystal structure. The crystal structure of NFS-(Ni/Fe:2/3)-CNT is in good

agreement with the formation of the (Fe₃NiS_{8-δ})^{-4+δ} structure, while NFS-(Ni/Fe:1/4)-CNT and NFS-(Ni/Fe:3/2)-CNT partly lose their crystal structures, and the XRD data of these catalysts suggested the formation of the Fe_{0.4}Ni_{3.6}S₈ phase (ICDD no. 03-065-33-25). As explained in XPS, C–S–C-doped CNTs can also assist the enhanced electrocatalytic activity, but as XRD of NFS-(Ni/Fe:2/3)-CNT (Figure 2a) showed that the intensity of carbon is negligible, the contribution by the C–S–C-doped (S-doped) CNT is not appreciable. Meanwhile, for FS-CNT, the Fe₉S₁₀ (ICDD no. 00-034-1470) and Fe₃S₄ (ICDD no. 01-089-1998) structures had formed, and hence, iron sulfide in this phase exhibited a

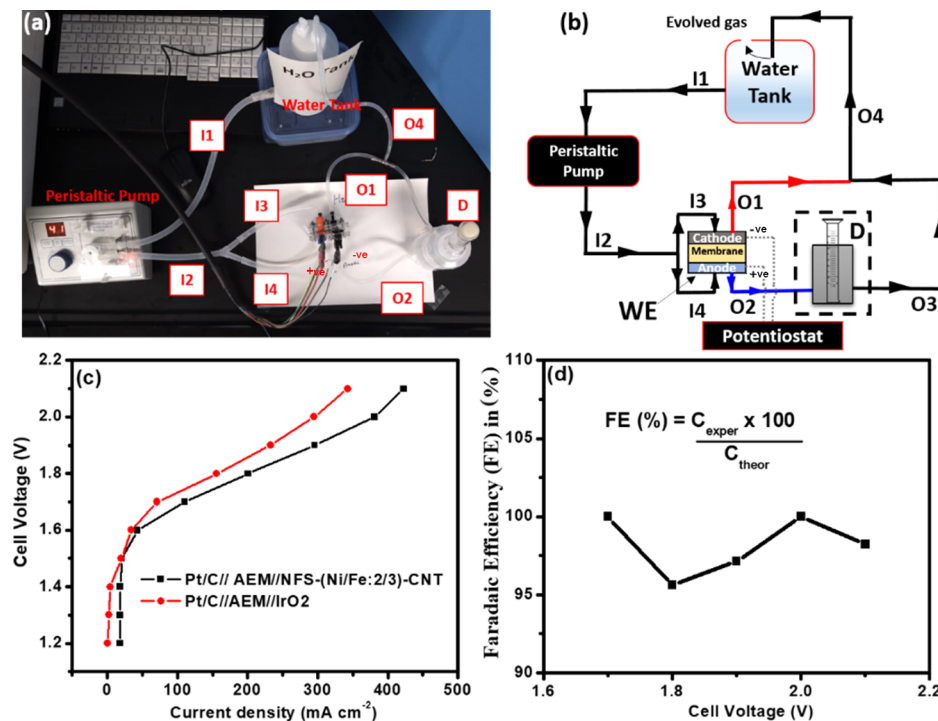
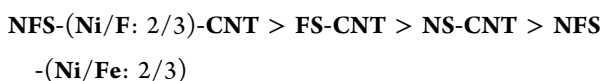


Figure 8. (a) Alkaline electrolyte membrane (AEM) electrolyzer display and (b) its flowchart diagram (note: I1 is the water inlet to the peristaltic pump, I2 is the water outlet from the peristaltic pump, and I3 and I4 are the water inlets for the anode and cathode of the AEM, respectively. O1 (red) and O2 (blue) are the water outlets for the anode with O_2 evolution and the cathode with H_2 evolution of the AEM, respectively. D is the water displacement setup to measure the amount of gas evolved, and O3 is the water outlet without gas evolution. O4 is the water recirculation line; the water tank is half-filled so that the gas can escape not to interfere with further water electrolyzer reaction. The potential (+ve and -ve in the diagram) was applied using potentiostatic power supply, and the corresponding current was recorded. WE is alkaline water electrolyzer assembly, and arrow marks in the line indicate the direction of the flow of water. (c) Plot of current density vs cell voltage and (d) FE of the AEM electrolyzer.

lower performance than NFS-(Ni/Fe:2/3)-CNT (Figure S4). The chronopotentiometric OER durability test of NFS-(Ni/Fe:2/3)-CNT was carried out, and the result is shown in Figure S3e, in which the catalyst activity is not much different even after 35 h, indicating the high durability of the catalyst.

In Table 2, we summarize the suggested crystal structures of the synthesized catalysts as well as the Ni and Fe oxidation states of the synthesized metal sulfide catalysts. Based on the half-wave potentials of the ORR and OER at 10 mA/cm², we calculated the oxygen electrode potential for NFS-(Ni/Fe:2/3)-CNT, NFS-(Ni/Fe:2/3), NS-CNT, and FS-CNT, which were 0.74, 1.00, 0.88, and 0.84 V, respectively.

In summary, the order of high bifunctional oxygen electrode performances is as follows



NFS-(Ni/Fe:2/3)-CNT with Fe in the +3-oxidation state forms the Fe_3NiS_8 structure (see Table 2), which exhibited high OER and ORR activities compared to the other catalysts. This behavior might be due to the point defects in the $(\text{Fe}_3\text{NiS}_{8-\delta})^{-4+\delta}$ structure that creates sulfur vacancies made by the self-interstitial structure of the nickel atom in the Fe_3NiS_8 structure of NFS-(Ni/F:2/3)-CNT, while the same interstitial structure of the Fe^{II} atom in the $(\text{Ni}_3\text{FeS}_{8-\delta})^{-8+\delta}$ structure of NFS-(Ni/Fe:2/3) leads to the formation of iron oxides as described based on the *in situ* electrochemical XRD data. NS-CNT and FS-CNT did not exhibit such point defects because of the absence of the interstitial transition atom. Furthermore,

based on the oxidation states of nickel, iron, and sulfides, we have concluded that the charge borne by the crystal structure of NFS-(Ni/Fe:2/3)-CNT is $(\text{Fe}_3\text{NiS}_{8-\delta})^{-4+\delta}$.

2.4. Zn–Air Battery Performance. Based on the obtained superior ORR and OER performance and durability of NFS-(Ni/Fe:2/3)-CNT, we used this catalyst as a cathode material for the Zn–air battery assembly. The Zn–air battery assembly was prepared by coating the catalysts on the carbon supports (Supporting Information, Section S1.2), and its performance is shown in Figure 7c–e. For comparison, we tested the battery performance using NFS-(Ni/Fe:2/3), which does not contain the CNTs as a cathode material. As can be seen in Figure 7c, NFS-(Ni/Fe:2/3)-CNT provides a specific capacity of 817 mA h/g, while the specific capacity of NFS-(Ni/Fe:2/3) was 52 mA h/g, which is much lower than that of NFS-(Ni/Fe:2/3)-CNT. Further, to understand the rate performance of the NFS-(Ni/Fe:2/3)-CNT catalysts at different current densities (5, 10, and 20 mA/cm²), we have found that the plateau voltages of NFS-(Ni/Fe:2/3)-CNT at the current densities of 5, 10, and 20 mA/cm² are 0.94, 1.06, and 1.16 V, respectively. This showed that increasing the current densities decreases the plateau voltage and discharging time, which confirms the long-term discharge capabilities at different current densities, which are comparable with those of the state-of-the-art catalysts reported.^{55–57} These results indicate that the CNTs are very important for such a high performance.

As already described, both NFS-(Ni/Fe:2/3)-CNT and NFS-(Ni/Fe:2/3) form the $(\text{Fe}_3\text{NiS}_{8-\delta})^{-4+\delta}$ structure, while the $(\text{Fe}_3\text{NiS}_{8-\delta})^{-4+\delta}$ formation cannot explain such a high

specific capacity difference. Figure 7d shows the current density versus voltage performances of the NFS-(Ni/Fe:2/3)-CNT and NFS-(Ni/Fe:2/3) electrodes, in which NFS-(Ni/Fe:2/3)-CNT shows much lower overpotential gaps between the charging and discharging compared to that of NFS-(Ni/Fe:2/3), although the overpotential increases with an increase in the current density. The rechargeable battery performances of the NFS-(Ni/Fe:2/3)-CNT and NFS-(Ni/Fe:2/3) electrodes are shown in Figures 7e and S5b, respectively. NFS-(Ni/Fe:2/3)-CNT initially exhibited discharging and charging at 1.21 and 1.90 V, respectively, and NFS-(Ni/Fe:2/3) provided a discharging voltage and a charging voltage of 0.45 and 1.96 V, respectively. Figure 7e shows the cyclability test of NFS-(Ni/Fe:2/3)-CNT, noting that it is durable for 1220 min. NFS-(Ni/Fe:2/3)-CNT (0.66 V) exhibited a charge and discharge potential difference of 0.66 V, which is lower compared to that of NFS-(Ni/Fe:2/3) (1.51 V), as shown in (Figure S5), suggesting that the Fe^{III} state in the $(\text{Fe}_3\text{NiS}_{8-\delta})^{-4+\delta}$ structure of NFS-(Ni/Fe:2/3)-CNT is important for the higher rechargeable battery performance compared to the Fe^{II} state in the $(\text{Ni}_3\text{FeS}_{8-\delta})^{-8+\delta}$ structure. However, after 1220 min, the overpotential gap between the charge and discharge increased (Figure 7e).

2.5. Alkaline Water Electrolyzer Performance. Figure 8a,c shows an alkaline water electrolyzer setup and its diagram. The membrane electrode assembly (MEA) was assembled using Pt/C//AEM//NFS-(Ni/Fe:2/3)-CNT, in which NFS-(Ni/Fe:2/3)-CNT acts as the anode and the state-of-the-art HER catalyst (Pt/C) was used as the cathode. The MEA with Pt/C//AEM//IrO₂ was also assembled, in which the state-of-the-art OER catalyst (IrO₂) and Pt/C were used as the anode and cathode, respectively, for comparison. The cell voltage of MEAs versus current density was measured, and the result is shown in Figure 8c. The MEA of Pt/C//AEM//NFS-(Ni/Fe:2/3)-CNT was found to show a current density of 297 mA/cm² at 1.9 V, which was much higher than that (237 mA/cm²) of the all-noble-metal MEA assembly of Pt/C//AEM//IrO₂ (see Figure 8c). It is evident that the NFS-(Ni/Fe:2/3)-CNT anode in the alkaline water electrolysis demonstrated a superior water electrolyzer performance.

In order to evaluate the faradaic efficiency (FE) of this system, we calculated the Coulombic efficiency from the obtained current during electrolysis for each voltage, which is expressed as theoretical Coulombic efficiency (see the Supporting Information, Figure S6), and the Coulombic efficiency was calculated using the amount of O₂ evaluated through the water displacement method (see D in Figure 8b), which is the experimental Coulombic efficiency. We calculated the FE of the cell based on the sluggish anodic O₂ evolution side. The calculation details of the theoretical and experimental Coulombic efficiencies are described in the Supporting Information, Figure S6 and Section S4. In order to estimate the amounts of O₂ and H₂ gases evolved from the lines O2 and O1, respectively, O₂ from the anode and H₂ from the cathode were examined by gas chromatography (GC) through GC syringe ejection from the siloxane septum in the water displacement setup (D) (Figure 8b), and for the GC measurement of the H₂ gas, the D setup was replaced in the O1 line of water circulation. To compare the relative purity of the O₂ and H₂ gases, we used commercial O₂, N₂, and H₂ gases. The commercial O₂ (Figure S7a) exhibits a small amount of H₂ in the gas chromatograph, which would be due to humidified water vapor in the measuring jar. The

commercial H₂ (Figure S7b) also shows a small amount of N₂ and O₂ because of the atmospheric N₂ and water vapor interference, and the standard N₂ shows a small amount of H₂ and O₂ because of the water vapor interference. Hence, although GC of O₂ (Figure S7c) and H₂ (Figure S7d) performed using the alkaline electrolyzer setup also shows the peaks from a small amount of water and atmospheric air contamination, O₂ and H₂ evolved from the present MEA are concluded to be pure. In order to evaluate the consistency of the electrolyzer, the FE was calculated (Table S3), and the result in the range of 1.7–2.1 V is shown in Figure 8d. The FE calculated using the equation put in the inlet in Figure 8d was between 97 and 99.98%. We emphasize that the obtained FE is very high.

2.6. In Situ XRD Analysis. In order to understand the structural changes and active sites of the catalysts, we carried out *in situ* electrochemical XRD measurements of the discharging and charging processes of NFS-(Ni/Fe:2/3)-CNT and NFS-(Ni/Fe:2/3), and the results are shown in Figures 9 and S8. To understand the lattice changes of each

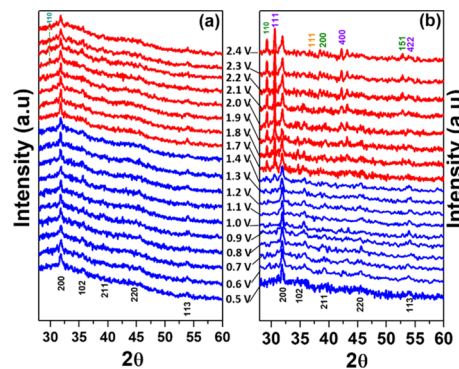


Figure 9. *In situ* electrochemical XRD patterns of (a) NFS-(Ni/Fe:2/3)-CNT during charging (red) and discharging (blue) and (b) NFS-(Ni/Fe:2/3) cathodes during charging (red) and discharging (blue).

atom in these structures, we focused on the major intensity peaks of the $(\text{Fe}_3\text{NiS}_{8-\delta})^{-4+\delta}$ and $(\text{Ni}_3\text{FeS}_{8-\delta})^{-8+\delta}$ structures of NFS-(Ni/Fe:2/3)-CNT and NFS-(Ni/Fe:2/3), respectively, which include the 200, 102, 211, 220, and 113 planes. The two-dimensional views of all these planes of the $(\text{Fe}_3\text{NiS}_{8-\delta})^{-4+\delta}$ structures through the unit cells are displayed in Figure S6, and the geometries of all the planes are discussed in the Supporting Information, Section S3. In Figure 9a, we observed, except for the 200 planes, shifts in the peaks during the discharging process. For the 102 planes, a gradual positive shift by 0.2° was observed during the discharging and charging voltages from 0.5 to 2.4 V. No such peak shift was observed on the 113 planes during the applied potential from 0.5 to 1.7 V (Figure 9a), while from 1.8 to 2.4 V, the peaks corresponding to the 113 planes shifted to 53.88°, which is not a drastic change. The other crystal planes of $(\text{Fe}_3\text{NiS}_{8-\delta})^{-4+\delta}$ such as the 111, 211, and 220 planes show a lower peak intensity because of the high charge and discharge currents. When using NFS-(Ni/Fe:2/3) as the cathode electrode for the Zn-air battery, as shown in Figure 9b, during discharging (from 0.5 to 1.4 V), no shift in the peak of the 200 planes was observed, while the other planes exhibited either no detectable peak shifts or a decreased intensity in the XRD patterns (Figure 9a).

Although Fe³⁺ in NFS-(Ni/Fe:2/3)-CNT strongly resists oxidation, there is a trace amount of the 110 plane of the

FeOOH phase which was observed above 2.1 V (dotted line in Figure 9a). Hence, as the number of cycles increases to 7 at 50 min of continuous charging/discharging voltages (Figure 7f), there is a trace amount of iron oxide formation (FeOOH) which slightly resists the electron-transfer rate and is ultimately responsible for consumption of a higher voltage to afford 10 mA/cm². After 50 min of charge/discharge (seventh cycle), there is steady charging voltage until 1200 min, which shows that oxide formation in the $(\text{Ni}_3\text{FeS}_{8-\delta})^{-8+\delta}$ structure of NFS-(Ni/Fe:2/3) is due to the uneven oxidation of Ni^{II} and Fe^{II} (Figure 6b,d). NFS-(Ni/Fe:2/3) did not exhibit a stable performance, probably because of the Fe^{II} oxidation producing various oxidation products, such as Ni_2FeO_4 , FeO, and FeOOH. Based on the XPS and *in situ* electrochemical XRD results, it is suggested that the Fe^{III} sites in NFS-(Ni/Fe:2/3)-CNT are not active sites; instead, the bonding of Fe^{III} with sulfur is important for the durability during the oxidation, and mostly, Fe³⁺ resists the oxidation during charging.

Unlike NFS-(Ni/Fe:2/3)-CNT, NFS-(Ni/Fe:2/3) (Figure 9b) exhibited peak shifts or a diminishing peak intensity in the XRD peaks of all the planes except for the 200 planes. As can be seen in Figure 9b, unlike the discharging process, during the charging process (potential applied from 1.7 to 2.4 V), there are additional peaks including the 111 (30.25°), 422 (54.45°), and 400 (43.20°) planes of Ni_2FeO_4 (violet color); 111 (36.00°) attributable to FeO (orange asterisk); and 200 (41.20°), 110 (30.01°), and 151 (52×10^0) planes of FeOOH (green asterisk) (structural details are listed in Table S4 using ICDD numbers). Such results indicated the charging and reductive (discharging) voltage processes. Furthermore, the standard electrode potential of Fe^{II} is 0.70 V versus RHE; hence, Fe^{III} in NFS-(Ni/Fe:2/3)-CNT is stable in the higher potential region of the alkaline environment, and its standard electrode potential is 0.24 V versus RHE; thus, the catalyst is stable under the oxidative and reductive conditions of the Zn–air battery. This is further confirmed by the *in situ* electrochemical Zn–air battery performance of NFS-(Ni/Fe:2/3) under the charging and discharging conditions (Figure 9b). Although NFS-(Ni/Fe:2/3) is active under the OER and ORR conditions in an alkaline environment (Figure 9b), it was difficult to maintain the performance because of its poor discharge capability of Fe^{II} sites and unstable ORR after repeated cycling.

2.7. Why is Fe^{III} Active and Stable? There are many reports describing the importance of sulfur vacancies responsible for the excellent electrocatalytic active sites.^{44,46} The stable half-filled Fe^{III} configuration in NFS-(Ni/Fe:2/3)-CNT exhibited less shielding of nuclear attraction and enabled to pull the electron cloud toward itself, which induces a slightly positive-charged character at nickel that favors easy adsorption and desorption of hydroxyl ions ($-\text{OH}^-$). NFS-(Ni/Fe:2/3)-CNT has a stable behavior because of the unusual valence state of Fe^{III}.³² Hence, Fe^{III} in NFS-(Ni/Fe:2/3)-CNT exhibited an electron transfer from sulfur to Fe because of self-doping. The p-orbital energy level of sulfur is close to or even higher than the initially empty d-levels of Fe; hence, a part of the sulfur p-electrons transfer to the d-levels, resulting in the formation of holes. This situation is called self-doping or a negative charge-transfer gap. However, there exists a hybridization between the p-sites of sulfur and d-states of Fe by the negative charge-transfer gap of Fe, which results in the modification of the formal $d^n\text{p}^6$ configuration to the $d^{n-1}\text{p}^6$ state (d–p mixing during ligation).^{32,34} Hence, sulfur is either bonded strongly

with Fe^{III} or creates vacant sites. We demonstrated the self-doping of Fe^{III} with sulfur rather than sulfur vacancies because of the vacancies created due to the holes created in the p-orbitals during d–p hybridization in Fe^{III} of NFS-(Ni/Fe:2/3)-CNT. Thus, Fe^{III} is highly stable as expected from the d–p hybridization of iron at the expense of either the sulfur vacancies or holes in the p-orbital of sulfur. Hence, not all the sulfur atoms bonded to the Fe^{III} atoms need to be vacant.^{32–34} This explains how the 200 plane of NFS-(Ni/Fe:2/3)-CNT is highly stable (Figure 9a) during the discharging and charging processes, while Fe^{II} in NFS-(Ni/Fe:2/3) is not stable (Figure 9b). As experimental STEM analysis and theoretical studies suggested, sulfur vacancies of NFS-(Ni/Fe:2/3)-CNT contribute mainly for the enhancement of catalytic activity. Hence, we calculated the number of sulfur vacancies per angstrom from the HAADF pattern from Figure 4, which provides quantified evidence to the effect of sulfur vacancies. We have found that there are 51 S-vacancies per 9 unit cells (286.29 Å² area) of the $(\text{Fe}_3\text{NiS}_{8-\delta})^{-4+\delta}$ crystal structure of NFS-(Ni/Fe:2/3)-CNT catalysts which is shown in Figure S10. Further, we have given theoretical evidence using DFT that surface-exposed S-vacancy sites are the active sites.

2.8. Theoretical Simulations. We have employed periodic, pseudopotential-based DFT calculations implemented in the Vienna ab initio software package (VASP) to elucidate the synergetic effect between the CNT and the Ni/Fe sulfides. The Perdew–Burke–Ernzerhof (PBE) exchange–correlation functional was applied using projector augmented wave pseudopotentials. The electron energies converged to 10⁻⁶ eV using systems and Fermi smearing with sigma = 0.1 eV. The calculations were performed with 400 eV. Because of the large size of the investigated systems, we have performed the calculations with γ -point sampling. The relaxation was performed until the forces converged to values below 0.03 eV/Å². Activation barriers for various reaction mechanisms were obtained using the nudged elastic band (NEB) method combined with the climbing nudged elastic band (cNEB) method.

Our first task was to elucidate the effect of the supporting carbon on the valence states of the transition metals in the Ni/Fe sulfides. Owing to the large diameter of the CNTs used in the experiment, the CNT surface curvature effect would be minimal. Thus, we prepared our models with Ni/Fe sulfides adsorbed on the graphene surface. The models are shown in Figure S9 (Supporting Information). We performed a Bader population analysis and electron density difference map calculations to elucidate the effect of the carbon support. Our analysis showed that as a result of the Ni/Fe sulfide deposition on the carbon surface, both Fe and Ni lose electron density, and the S electron density remains unchanged, while the C atoms gain electron density. The detailed charge analysis is shown in Figure S9. The reduced electron density of the transition metals manifests in easier formation of the S-vacancy in order to maintain the charge neutrality of the system. We consider these surface-exposed S-vacancy sites as the active sites for the ORR mechanism investigated here.

2.9. Mechanism of OER and ORR Using *In Situ* FT-IR and Theoretical Calculations. Figure 10 shows the proposed mechanism for the ORR on the carbon-supported Ni/Fe sulfides with the CNT support. The oxygen molecule is adsorbed onto a surface-exposed S-vacancy site (step 1 in Figure 11). As a result, the electron density is transferred from the transition metals to the dioxygen, resulting in the formation

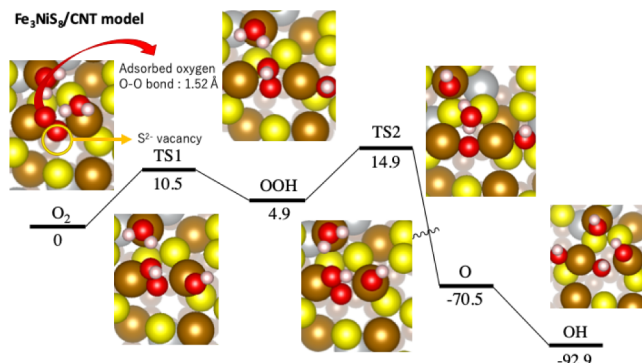


Figure 10. Reaction mechanism and the reaction energy diagram for ORR on carbon-supported Ni/Fe sulfides. All energies are in kilocalories per mole. Fe is denoted by brown, Ni is denoted by silver, S is denoted by yellow, O is denoted by red, and H is denoted by white.

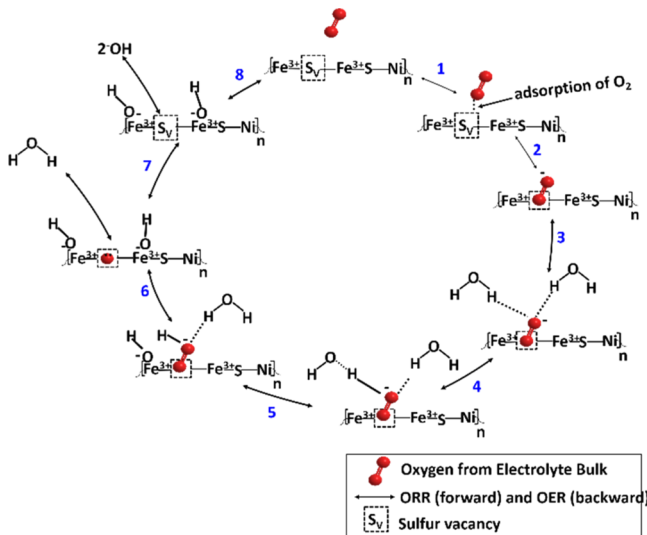
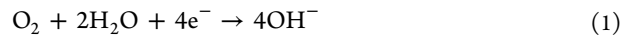


Figure 11. Pictorial representation of the ORR and OER mechanisms based on the theoretical studies shown in Figure 9.

of surface peroxy species (step 2 in Figure 11) with the O–O bond length of 1.52 Å. The surface peroxy species is stabilized by coordination with two water molecules *via* hydrogen bonds

(step 3 in Figure 11). In the initial reaction step, the peroxy species extracts a hydrogen atom from a water molecule, resulting in a surface hydro-peroxy species (step 4 in Figure 11) and a surface hydroxyl group (step 5 in Figure 11). The activation barrier for this process is 10.5 kcal/mol, and the resulting intermediate hydro-peroxy species is 4.9 kcal/mol higher in energy. In a second reaction step, the hydro-peroxy species extracts a hydrogen atom from the second water molecule, leading to the formation of one water molecule, a second hydroxyl group, and a surface oxo species (step 6 in Figure 11). The second reaction step is characterized with an activation barrier of 10 kcal/mol, and the products are stabilized with 70.5 kcal/mol relative to the initial reactants. In the final step, the surface oxo species extracts a hydrogen atom from the water molecule and two more hydroxyl groups are formed. The final product is stabilized with 92.9 kcal/mol with respect to the initial reactants (step 8 in Figure 11). The overall reaction can be summarized by the following energy equation (eq 1)



Step 8 implies that the process continues with initial step 1 during the reaction.

To elucidate the effect of the supporting carbon, we have tested the ORR mechanism on the free-standing Ni/Fe sulfides using theoretical simulations. The reaction steps and its energetics are shown in Figure 12. In the first step, the formation of hydro-peroxy species proceeds similar to the carbon-supported sulfides.

However, in the second step, the actual O–O bond cleavage requires a high activation barrier compared to the carbon-supported sulfides. The activation barrier for TS2 is estimated to be 14.1 kcal/mol, which is higher than 10 kcal/mol for the carbon-supported sulfides. Finally, the most stable product on the unsupported sulfides is the surface oxo species and two hydroxyl groups. The interaction of the surface oxo species with a second water molecule is an uphill reaction of 44.7 kcal/mol.

Based on the theoretical studies, we propose a mechanism for the Zn–air battery and water electrolyzers, as shown in Figures 7f and 11. The cleavage of the O–O bond in the second step is facile on NFS-(Ni/Fe:2/3)-CNT with a low activation barrier (step 5 in Figure 11), while this is a difficult

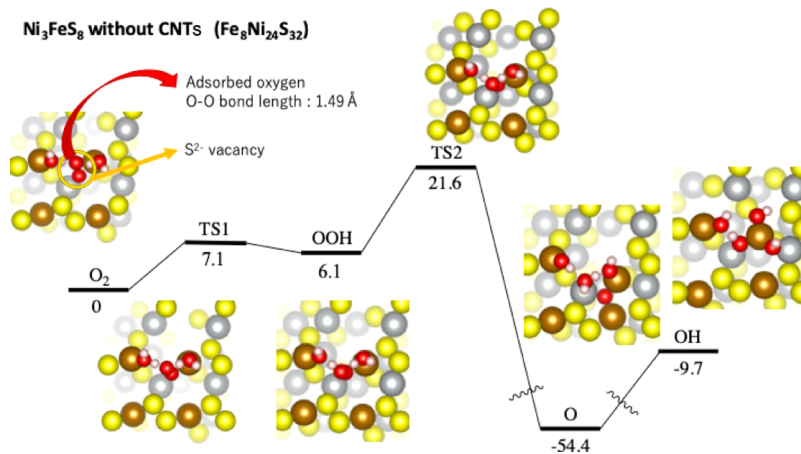


Figure 12. Reaction mechanism and the reaction energy diagram for ORR free-standing Ni/Fe sulfides. All energies are in kilocalories per mole. Fe is denoted by brown, Ni is denoted by silver, S is denoted by yellow, O is denoted by red, and H is denoted by white.

step for NFS-(Ni/Fe:2/3) because of its high activation barrier. This supports the oxidation of iron (FeO, FeOOH, and Ni_2FeO_4) (see Figure 9b and Table S4) during the charge–discharge of NFS-(Ni/Fe:2/3), while the behavior is less dominant in the *in situ* XRD of NFS-(Ni/Fe:2/3)-CNT (Figure 9a, step 5 in Figure 11).

Here, we carried out *in situ* electrochemical FT-IR measurements to support experimentally the mechanism of OER and ORR of the catalysts based on the theoretical approaches on the ORR mechanism. Figure 13a,b shows the *in*

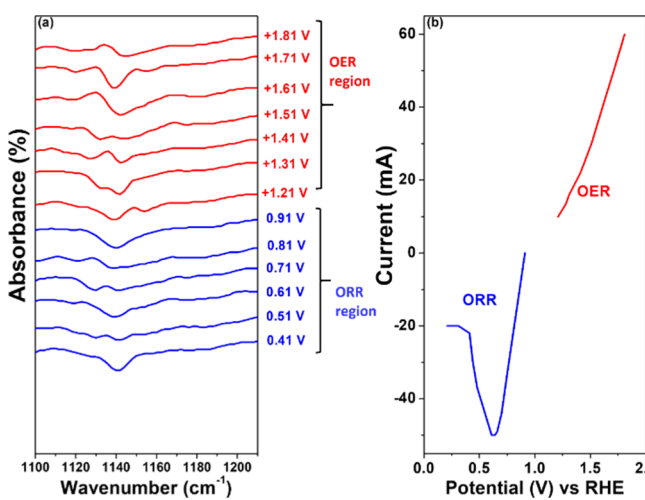


Figure 13. (a) *In situ* electrochemical FT-IR spectra of NFS-(Ni/Fe:2/3)-CNT during potential sweeps (potential vs RHE) in the ORR (blue) and OER (red) regions. (b) Corresponding current vs potential curve of NFS-(Ni/Fe:2/3)-CNT during the *in situ* electrochemical FT-IR measurements (blue for the ORR region and red for the OER region).

situ electrochemical FT-IR spectra of NFS-(Ni/Fe:2/3)-CNT during potential sweeps in the ORR and OER regions, in which the FT-IR frequencies of the O–O vibrations at their corresponding voltages are listed in Table S5.

In the OER region (red curves in Figure 13a,b), we also observed the following features: (i) at the initial potential (1.21 V), the O–O vibrational frequencies appeared at higher wavenumbers of 1153.83 (solvated O_2) and 1139.25 cm⁻¹ (superoxide ion O_2^-), which closely support step 1 (Figure 11) of the theoretical prediction. (ii) When the potential increases from 1.31 to 1.41 V, the wavenumbers of solvated O_2 and the superoxide ion shifted to a lower wavenumber (Figure 13a,b)

and Table S5), which suggested that the potential increase until 1.41 V promotes the solvated O_2 formation and supports the existence of hydroxo species at the NFS-(Ni/Fe:2/3)-CNT surfaces, which strongly supports steps 2, 3, and 4 of the theoretical prediction (Figure 11). (iii) When the potential increases from 1.51 to 1.81 V, the frequencies of both solvated O_2 and the superoxide ion shifted to higher wavenumbers (see Figure 13a and Table S5), which would be due to the strong adsorption of solvated O_2 on the catalyst and the superoxide ion (O_2^-) that would lead to high OER performance.

Based on the result of the ORR region (blue curves in Figure 13a,b), the important features are as follows: (i) from the initial ORR applied potential in the range of −0.91 to −0.41 V, we observed solvated O–O vibrations at ~1140 cm⁻¹ (see step 1 of Figure 11, see Table S5). In this potential range, the ORR current is very low compared to the other ORR potentials (Figure 13b). (ii) In the potential range of −0.81 to −0.51 V, solvated O–O vibrations appeared in the range of 1127–1140 cm⁻¹ (see Table S5 for each potential), which are associated with the superoxide O–O vibrations in the range of 1120–1125 cm⁻¹ (see Table S5 for each potential). Hence, steps 1 and 2 of the reaction mechanism in Figure 11 are suggested to involve the solvated O_2 molecules for NFS-(Ni/Fe:2/3)-CNT. (iii) The obtained results indicated that the ORR is accelerated during the potential range of −0.81 to −0.51 V (Figure 13a,b). Meanwhile, when the ORR potentials gradually decreased from −0.81 to −0.51 V, both the solvated O_2 vibrations and superoxide (O_2^-) vibrations shifted to slightly higher frequencies (Table S5), which would increase the strength of the O–O vibrational frequencies. In contrast, the O–O stretching frequencies in the lower-current region (−0.91 and −0.51 V) shifted to a lower-frequency region, which indicates the involvement of solvated O_2 molecules less appreciable and supports step 1 of the reaction mechanism (Figure 11). We evaluated the ORR and OER Tafel slopes of NFS-(Ni/Fe:2/3)-CNT, and the result is shown in Figure 14. For comparison, the Tafel slopes of RuO₂ and Pt/C are also displayed. As can be seen in Figure 14a, the OER Tafel slopes of NFS-(Ni/Fe:2/3)-CNT are different (55 mV dec⁻¹ and 75 mV dec⁻¹) in the potential regions of 1.35–1.53 and 1.55–1.78 V. Both Tafel slopes were lower than that of the state-of-art-RuO₂ catalysts which exhibited 96 mV dec⁻¹, which indicated fast OER electrode kinetics on NFS-(Ni/Fe:2/3)-CNT. Together with the *in situ* FT-IR results and theoretical studies (Figures 10–13), we may explain the two different Tafel slopes shown in Figure 14a as follows: (i) the Tafel slope of 55 mV dec⁻¹ in the lower OER potential region (1.33–1.48 V) and a low

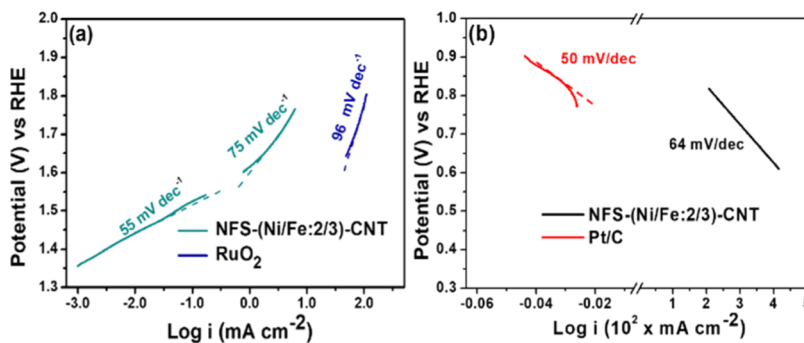


Figure 14. Tafel plots of NFS-(Ni/Fe:2/3)-CNT in the potential regions of (a) OER and (b) ORR. Tafel slopes of RuO₂ (a) and Pt/C (b) are also shown for comparison.

activation barrier for the O–O cleavage within the *in situ* FT-IR and theoretical calculation discussions at the potentials (1.31–1.41 V) and (ii) the Tafel slope of 75 mV dec⁻¹ for the potential region (1.58–1.79 V) in the higher OER potential region suggested main dominance by formation of oxides, which is in good agreement with wavenumber shifts in the *in situ* FT-IR discussion at the potential region of 1.51–1.81 V, and high activation barriers in the O–O cleavage in the final steps of the reaction mechanism. For the ORR, as shown in Figure 14b, the Tafel slope of NFS-(Ni/Fe:2/3)-CNT is 64 mV dec⁻¹, which is slightly greater than that of conventional state-of-the-art catalysts, that is, Pt/C (50 mV dec⁻¹).

We summarize the following important features: (i) Fe^{III} in the CNT-nickel iron sulfide hybrid catalyst exhibits higher OER and ORR activities and durability compared to the other catalysts, and the Fe^{III} sites in NFS-(Ni/Fe:2/3)-CNT are stable; meanwhile, the Fe^{II} sites in NFS-(Ni/Fe:2/3) are not stable. (ii) NFS-(Ni/Fe:2/3)-CNT with the $(\text{Fe}_3\text{NiS}_{8-\delta})^{-4+\delta}$ structure has many sulfur vacancies. (iii) The activation barriers for the O–O cleavage in step 5 of Figure 11 of OER and ORR mechanisms are suggested for the high Zn–air battery and anodic water electrolyzer performances of NFS-(Ni/Fe:2/3)-CNT.

We now present a plausible structure and activity relationship for high electrochemical performance of NFS-(Ni/Fe:2/3)-CNT as follows: (i) if the charge and discharge processes occur at the lower voltages (1.31–1.41 V), a low activation barrier for step 5 of Figure 11 dominates in NFS-(Ni/Fe:2/3)-CNT and leads to the formation of the solvated O₂ molecule to facilitate the easy formation of oxo species. (ii) The sulfur vacancies (step 1 of Figure 11) near the Fe^{III} of $(\text{Fe}_3\text{NiS}_{8-\delta})^{-4+\delta}$ structure provide adequate sites for the oxo species formation (step 2 of Figure 11), leading to a faster reaction and stable electrode kinetics. (iii) In contrast, a higher-voltage mechanism dominates with the formation of oxides instead of oxo species formation from water because of the high activation barrier in step 5 of Figure 11 and favors the formation of the oxides, which may partially restrict effective electron flow. Such an explanation explains why the Zn–air battery charge–discharge overpotentials increase after a 1220 min operation (Figure 7f) because during long cycles at a constant current density (10 mA/cm²), NFS-(Ni/Fe:2/3)-CNT exhibits a large discharge–charge overpotential gap.

3. CONCLUSIONS

We have designed and synthesized novel iron–nickel–sulfide/CNT hybrids by changing the Ni/Fe ratios and found that in the NFS-(Ni/Fe:2/3)-CNT catalyst, iron forms the Fe^{III} valence state and has the $(\text{Fe}_3\text{NiS}_{8-\delta})^{-4+\delta}$ crystal structure. The obtained Fe^{III}-doped nickel sulfide/CNT hybrid catalyst exhibited a very high ORR ($E_{1/2} = 0.82$ V), OER (potential at 10 mA/cm² = 1.55 V), and Zn–air battery and water electrolyzer performances. The molar ratios of nickel thiourea and iron thiourea in the complexes as well as hybrid formation with CNTs were highly important in the synthesis of such a catalyst with very high electrochemical performances. The *in situ* electrochemical XRD study of the catalyst concluded that the 200 plane of Fe₃NiS₈ is highly stable under alkaline conditions and responsible for creating the sulfur vacancies in the crystal sites, and the Fe^{III} state in NFS-(Ni/Fe:2/3)-CNT was a key component for such an enhanced and durable discharging (ORR) and charging (OER) performance of the Zn–air battery. The analyzed *in situ* electrochemical FT-IR

and Tafel plot showed that the low activation barrier of the hydroxo species is responsible for the outstanding charge and discharge behavior. Both *in situ* electrochemical FT-IR and XRD characterization concluded that iron doping with the nickel sulfides in the +3 oxidation state enhanced the OER and ORR catalytic activities. Such results should be highly important and useful for the development of a rechargeable and durable Zn–air battery and alkaline water electrolyzer with a high performance for real-world applications.

Our experimental findings were elucidated using first-principles calculations. The theoretical results showed that the CNT support successfully stabilizes the Fe^{III} valence state and thus promotes the catalytic activity. The ORR mechanisms were compared for the CNT-supported sulfides and free-standing sulfides, verifying the crucial role of the carbon support. The CNT support helps in lowering of the activation barriers for the O–O bond cleavage. It also stabilizes the surface S-vacancy sites and promotes the reaction to the final products.

■ ASSOCIATED CONTENT

SI Supporting Information

The Supporting Information is available free of charge at <https://pubs.acs.org/doi/10.1021/acsaem.0c01931>.

Synthesis of catalysts, metal sulfides, materials and methods, electrochemical measurement details, crystal simulation details, control sample XRD, electrochemical performance and battery performances, plane details of *in situ* XRD, and *in situ* FT-IR frequency details (PDF)

■ AUTHOR INFORMATION

Corresponding Authors

Pandian Ganesan – International Institute for Carbon-Neutral Energy Research (I2CNER), Kyushu University, Fukuoka 819-0395, Japan;  orcid.org/0000-0003-2449-8096; Email: pandian.ganesan.631@m.kyushu-u.ac.jp

Naotoshi Nakashima – International Institute for Carbon-Neutral Energy Research (I2CNER), Kyushu University, Fukuoka 819-0395, Japan;  orcid.org/0000-0002-7890-4531; Email: nakashima.natashi.614@m.kyushu-u.ac.jp

Authors

Aleksandar Staykov – International Institute for Carbon-Neutral Energy Research (I2CNER), Kyushu University, Fukuoka 819-0395, Japan;  orcid.org/0000-0003-2572-1317

Hiroaki Shu – Zeon Corporation, Chiyoda-ku, Tokyo 100-8246, Japan

Mitsugu Uejima – Zeon Corporation, Chiyoda-ku, Tokyo 100-8246, Japan

Complete contact information is available at: <https://pubs.acs.org/10.1021/acsaem.0c01931>

Author Contributions

P.G. and N.N. designed the concept and conceived the experiments. P.G. carried out the experiments and analyzed the results. A.S. performed computer calculations. All authors discussed the results. P.G., N.N., and A.S. (calculation parts) wrote the paper.

Notes

The authors declare no competing financial interest.

ACKNOWLEDGMENTS

This study was supported by Zeon Corporation and the JSPS KAKENHI grant number P16H02083 (for N.N.).

ABBREVIATIONS

HAADF	high-angle annular dark field
XPS	X-ray photoelectron spectroscopy
STEM	scanning transmission electron microscopy
TEM	transmission electron microscopy
FT-IR	Fourier transform infrared
CNT	carbon nanotube
DFT	density functional theory
cNEB	climbing nudged elastic band
NEB	nudged elastic band
ORR	oxygen reduction reaction
OER	oxygen evolution reaction
Pt	platinum
RuO ₂	ruthenium oxide
Zn-air battery	zinc–air battery

REFERENCES

- (1) Wang, J.; Cui, W.; Liu, Q.; Xing, Z.; Asiri, A. M.; Sun, X. Recent progress in cobalt-based heterogeneous catalysts for electrochemical water splitting. *Adv. Mater.* **2016**, *28*, 215–230.
- (2) Li, Y.; Zhou, Y.; Wen, H.; Yang, J.; Maouche, C.; Liu, Q.; Wu, Y.; Cheng, C.; Zhu, J.; Cheng, X. N,S-Atom-coordinated Co₉S₈ trinary dopants within a porous graphene framework as efficient catalysts for oxygen reduction/evolution reactions. *Dalton Trans.* **2018**, *47*, 14992–15001.
- (3) Zhou, D.; Jia, Y.; Yang, H.; Xu, W.; Sun, K.; Zhang, J.; Wang, S.; Kuang, Y.; Liu, B.; Sun, X. Boosting oxygen reaction activity by coupling sulfides for high-performance rechargeable metal-air battery. *J. Mater. Chem. A* **2018**, *6*, 21162–21166.
- (4) Lu, Y.-T.; Chien, Y.-J.; Liu, C.-F.; You, T.-H.; Hu, C.-C. Active site-engineered bifunctional electrocatalysts of ternary spinel oxides, M_{0.1}Ni_{0.9}Co₂O₄ (M: Mn, Fe, Cu, Zn) for the air electrode of rechargeable Zinc-air batteries. *J. Mater. Chem. A* **2017**, *5*, 21016–21026.
- (5) Ooka, H.; Yamaguchi, A.; Takashima, T.; Hashimoto, K.; Nakamura, R. Efficiency of Oxygen Evolution on Iridium Oxide Determined from the pH Dependence of Charge Accumulation. *J. Phys. Chem. C* **2017**, *121*, 17873–17881.
- (6) Damjanovic, A.; Brusic, V. Electrode kinetics of oxygen reduction on oxide-free platinum electrodes. *Electrochim. Acta* **1967**, *12*, 615–628.
- (7) Iwase, K.; Kamiya, K.; Miyayama, M.; Hashimoto, K.; Nakanishi, S. Sulfur-linked covalent triazine frameworks doped with coordinatively unsaturated Cu(I) as electrocatalysts for oxygen reduction. *ChemElectroChem* **2018**, *5*, 805–810.
- (8) Kakizaki, H.; Ooka, H.; Hayashi, T.; Yamaguchi, A.; Bonnet-Mercier, N.; Hashimoto, K.; Nakamura, R. Evidence that crystal facet orientation dictates oxygen evolution intermediates on rutile manganese oxide. *Adv. Funct. Mater.* **2018**, *28*, 1706319.
- (9) Wu, H.-L.; Huff, L. A.; Gewirth, A. A.; Gewirth, A. In situ Raman spectroscopy of sulfur speciation in Lithium-sulfur batteries. *ACS Appl. Mater. Interfaces* **2015**, *7*, 1709–1719.
- (10) Zhang, R.; Pan, C.; Nuzzo, R. G.; Gewirth, A. A. CoS₂ as a sulfur redox-active cathode material for high-capacity nonaqueous Zn batteries. *J. Phys. Chem. C* **2019**, *123*, 8740–8745.
- (11) Chen, W.; Wang, H.; Li, Y.; Liu, Y.; Sun, J.; Lee, S.; Lee, J.-S.; Cui, Y. In situ electrochemical oxidation tuning of transition metal disulfides to oxides for enhanced water oxidation. *ACS Cent. Sci.* **2015**, *1*, 244–251.
- (12) Ganesan, P.; Prabu, M.; Sanetuntikul, J.; Shanmugam, S. Cobalt sulphide nanoparticles grown on nitrogen and sulfur codoped graphene oxide: efficient for oxygen reduction and evolution reaction. *ACS Catal.* **2015**, *5*, 3625–3637.
- (13) Ganesan, P.; Sivanantham, A.; Shanmugam, S. Inexpensive electrochemical synthesis of nickel iron sulphides on nickel foam: super active and ultra-durable electrocatalysts for alkaline electrolyte membrane water electrolysis. *J. Mater. Chem. A* **2016**, *4*, 16394–16402.
- (14) Liu, H.; Ma, F.-X.; Xu, C.-Y.; Yang, L.; Du, Y.; Wang, P.-P.; Yang, S.; Zhen, L. Sulfurizing-Induced Hollowing of Co₉S₈ Microplates with Nanosheet Units for Highly Efficient Water Oxidation. *ACS Appl. Mater. Interfaces* **2017**, *9*, 11634–11641.
- (15) Zhao, W.; Zhang, C.; Geng, F.; Zhuo, S.; Zhang, B. Nanoporous hollow transition metal chalcogenide nanosheets synthesized via the anion-exchange reaction of metal hydroxides with chalcogenide ions. *ACS Nano* **2014**, *8*, 10909–10919.
- (16) *Nanocarbons for Energy Conversion-Supramolecular Approaches*; Nakashima, N., Ed.; Springer, 2018; pp 1–564.
- (17) Yang, J.; Ganesan, P.; Ishihara, A.; Nakashima, N. Carbon nanotube-based non-precious metal electrode catalysts for fuel cells, water splitting and zinc-air batteries. *ChemCatChem* **2019**, *11*, 5929–5944.
- (18) Chen, W.; Liu, Y.; Li, Y.; Sun, J.; Qiu, Y.; Liu, C.; Zhou, G.; Cui, Y. In situ electrochemically derived nanoporous oxides from transition metal dichalcogenides for active oxygen evolution catalysts. *Nano Lett.* **2016**, *16*, 7588–7596.
- (19) Feng, L.-L.; Fan, M.; Wu, Y.; Liu, Y.; Li, G.-D.; Chen, H.; Chen, W.; Wang, D.; Zou, X. Metallic Co₉S₈ nanosheets grown on carbon cloth as efficient binder-free electrocatalysts for the hydrogen evolution reaction in neutral media. *J. Mater. Chem. A* **2016**, *4*, 6860–6867.
- (20) Li, Q.; Xing, Z.; Wang, D.; Sun, X.; Yang, X. In situ electrochemically activated CoMn-S@NiO/CC nanosheets array for enhanced hydrogen evolution. *ACS Catal.* **2016**, *6*, 2797–2801.
- (21) Geng, D.; Ding, N.-N.; Hor, T. S. A.; Chien, S. W.; Liu, Z.; Zong, Y. Cobalt sulfide nanoparticles impregnated nitrogen and sulfur co-doped graphene as bifunctional catalyst for rechargeable Zn-air batteries. *RSC Adv.* **2015**, *5*, 7280–7284.
- (22) Wu, X.; Han, X.; Ma, X.; Zhang, W.; Deng, Y.; Zhong, C.; Hu, W. Morphology-controllable synthesis of Zn-CO-mixed sulphide nanostructures on carbon fibre paper toward efficient rechargeable Zinc-air batteries and water electrolysis. *ACS Appl. Mater. Interfaces* **2017**, *9*, 12574–12583.
- (23) Yang, H.; Wang, B.; Li, H.; Ni, B.; Wang, K.; Zhang, Q.; Wang, X. Trimetallic sulphide mesoporous nanospheres as superior electrocatalysts for rechargeable Zn-air batteries. *Adv. Energy Mater.* **2018**, *8*, 1801839.
- (24) Chandrasekaran, S.; Yao, L.; Deng, L.; Bowen, C.; Zhang, Y.; Chen, S.; Lin, Z.; Peng, F.; Zhang, P. Recent advances in metal sulphides: from controlled fabrication to electrocatalytic, photocatalytic and photoelectrochemical water splitting and beyond. *Chem. Soc. Rev.* **2019**, *48*, 4178–4280.
- (25) De, S.; Zhang, J.; Luque, R.; Yan, N. Ni-based bimetallic heterogeneous catalysts for energy and environmental applications. *Energy Environ. Sci.* **2016**, *9*, 3314–3347.
- (26) Faber, M. S.; Jin, S. Earth-abundant inorganic electrocatalysts and their nanostructures for energy conversion applications. *Energy Environ. Sci.* **2014**, *7*, 3519–3542.
- (27) Higgins, D.; Zamani, P.; Yu, A.; Chen, Z. The application of graphene and its composites in oxygen reduction electrocatalysis: a perspective and review of recent progress. *Energy Environ. Sci.* **2016**, *9*, 357–390.
- (28) Jiang, J.; Lu, S.; Wang, W.-K.; Huang, G.-X.; Huang, B.-C.; Zhang, F.; Zhang, Y.-J.; Yu, H.-Q. Ultrahigh electrocatalytic oxygen evolution by iron-nickel sulfide nanosheets/reduced graphene oxide nanohybrids with an optimized autoxidation process. *Nano Energy* **2018**, *43*, 300–309.
- (29) Jin, Y.; Yue, X.; Du, H.; Wang, K.; Huang, S.; Shen, P. K. One-step growth of nitrogen-decorated iron-nickel sulfide nanosheets for the oxygen evolution reaction. *J. Mater. Chem. A* **2018**, *6*, 5592–5597.

- (30) Su, C.-Y.; Cheng, H.; Li, W.; Liu, Z.-Q.; Li, N.; Hou, Z.; Bai, F.-Q.; Zhang, H.-X.; Ma, T.-Y. Zinc-air Batteries: atomic modulation of FeCo-nitrogen-carbon bifunctional oxygen electrodes for rechargeable and flexible all-solid state zinc-air battery. *Adv. Energy Mater.* **2017**, *7*, 1602420.
- (31) Wang, T.; Nam, G.; Jin, Y.; Wang, X.; Ren, P.; Kim, M. G.; Liang, J.; Wen, X.; Jang, H.; Han, J.; Huang, Y.; Li, Q.; Cho, J. NiFe(oxy) hydroxides derived from NiFe disulfides as an efficient oxygen evolution catalyst for rechargeable Zn-air batteries: The effect of surface S residues. *Adv. Mater.* **2018**, *30*, 1800757.
- (32) Streltsov, S. S.; Shorikov, A. O.; Skornyakov, S. L.; Poteryaev, A. I.; Khomskii, D. I. Unexpected 3+ valence of iron in FeO_2 , a geologically important material lying “in between” oxides and peroxides. *Sci. Rep.* **2017**, *7*, 13005.
- (33) Schlegel, A.; Wachter, P. Optical properties, phonons and electronic structure of iron pyrites (FeS_2). *J. Phys. C: Solid State Phys.* **1976**, *9*, 3363–3369.
- (34) Ribeiro, B.; Godinho, M.; Cardoso, C.; Borges, R. P.; Gasche, T. P. *J. Appl. Phys.* **2013**, *113*, 083906.
- (35) Ha, Y.; Oberst, J. L.; Zeng, Z.; Hoang, T. T. H.; Cohen, Y.; Wetzel, D. J.; Nuzzo, R. G.; Greeley, J.; Gewirth, A. A. In situ surface stress measurement and computational analysis examining the oxygen reduction reaction on Pt and Pd. *Electrochim. Acta* **2018**, *260*, 400–406.
- (36) Cheng, J.; Yang, J.; Kitano, S.; Juhasz, G.; Higashi, M.; Sadakiyo, M.; Kato, K.; Yoshioka, S.; Sugiyama, T.; Yamauchi, M.; Nakashima, N. Impact of Ir-vaence control and surface nanostructure on oxygen evolution reaction over a highly efficient Ir-TiO₂ Nanorod catalyst. *ACS Catal.* **2019**, *9*, 6974–6986.
- (37) Yang, J.; Fujigaya, T.; Nakashima, N. Decorating unoxidized-carbon nanotubes with homogeneous Ni-Co spinel nanocrystals show superior performance for oxygen evolution/reduction reactions. *Sci. Rep.* **2017**, *7*, 45384.
- (38) Yang, J.; Toshimitsu, F.; Yang, Z.; Fujigaya, T.; Nakashima, N. Pristine carbon nanotube/iron phthalocyanine hybrids with a well-defined nanostructure show excellent efficiency and durability for the oxygen reduction reaction. *J. Mater. Chem. A* **2017**, *5*, 1184–1191.
- (39) Miyadai, T. Weakferromagnetism in $\text{Fe}_x\text{Ni}_{1-x}\text{S}_2$ ($x=0\text{--}0.075$). *J. Magn. Magn. Mater.* **1979**, *10*, 29–33.
- (40) Andersson, K.; Nyberg, M.; Ogasawara, H.; Nordlund, D.; Kendelevicz, T.; Doyle, C. S.; Brown, G. E.; Pettersson, L. G. M.; Nilsson, A. Experimental and theoretical characterization of the structure of defects at the pyrite $\text{FeS}_2(100)$ surface. *Phys. Rev. B: Condens. Matter Mater. Phys.* **2004**, *70*, 195404.
- (41) Ding, Q.; Czech, K. J.; Zhao, Y.; Zhai, J.; Hamers, R. J.; Wright, J. C.; Jin, S. Basal-plane ligand functionalization on semiconducting 2H-MoS₂ monolayers. *ACS Appl. Mater. Interfaces* **2017**, *9*, 12734–12742.
- (42) Donarelli, M.; Bisti, F.; Perrozzi, F.; Ottaviano, L. Tunable sulfur desorption in exfoliated MoS₂ by means of thermal annealing in ultra-high vacuum. *Chem. Phys. Lett.* **2013**, *588*, 198–202.
- (43) Liu, S.; Wang, Z.; Zhou, S.; Yu, F.; Yu, M.; Chiang, C.-Y.; Zhou, W.; Zhao, J.; Qiu, J. Metal-organic framework-derived hybrid carbon nanocages as a bifunctional electrocatalyst for oxygen reduction and evolution. *Adv. Mater.* **2017**, *29*, 1700874.
- (44) Yang, M.-Q.; Wang, J.; Wu, H.; Ho, G. W. Noble Metal-free nanocatalysts with vacancies for electrochemical water splitting. *Small* **2018**, *14*, 1703323.
- (45) Meng, Z.; Wei, F.; Ma, W.; Yu, N.; Wei, P.; Wang, Z.; Tang, Y.; Chen, Z.; Wang, H.; Zhu, M. Design and synthesis of “all-in-one” multifunctional FeS₂ nanoparticles for magnetic resonance and near-infrared imagining guided photothermal therapy of tumours. *Adv. Funct. Mater.* **2016**, *26*, 8231–8242.
- (46) Fan, J.-J.; Fan, Y.-J.; Wang, R.-X.; Xiang, S.; Tang, H.-G.; Sun, S.-G. A novel strategy for the synthesis of sulfur-doped carbon nanotubes as a highly efficient Pt catalyst support toward the methanol oxidation reaction. *J. Mater. Chem. A* **2017**, *5*, 19467–19475.
- (47) Davidson, A.; Tempere, J. F.; Che, M.; Roulet, H.; Dufour, G. Spectroscopic studies of Nickel (II) and Nickel (III) species generated upon thermal treatments of Nickel/Ceria-supported Materials. *J. Phys. Chem. A* **1996**, *100*, 4919–4929.
- (48) Chang, H.-C.; Lin, S.-H.; Hsu, Y.-C.; Jen, S.-W.; Lee, W.-Z. Nickel(iii)-mediated oxidative cascades from a thiol-bearing nickel(ii) precursor to the nickel(iv) product. *Dalton Trans.* **2018**, *47*, 3796–3802.
- (49) Grosvenor, A. P.; Biesinger, M. C.; Smart, R. S. C.; McIntyre, N. S. New interpretations of XPS spectra of nickel metal and oxides. *Surf. Sci.* **2006**, *600*, 1771–1779.
- (50) Shi, J.; Li, X.; He, G.; Zhang, L.; Li, M. Electrodeposition of high-capacitance 3D CoS/graphene nanosheets on nickel foam for high-performance aqueous asymmetric supercapacitors. *J. Mater. Chem. A* **2015**, *3*, 20619–20626.
- (51) Luo, J. T.; Yang, Y. C.; Zhu, X. Y.; Chen, G.; Zeng, F.; Pan, F. Enhanced electromechanical response of Fe-doped ZnO films by modulating the chemical state and ionic size of the Fe. *Phys. Rev. B: Condens. Matter Mater. Phys.* **2010**, *82*, 014116.
- (52) Yamashita, T.; Hayes, P. Analysis of XPS spectra of Fe²⁺ and Fe³⁺ ions in oxide materials. *Appl. Surf. Sci.* **2008**, *254*, 2441–2449.
- (53) Luo, Y.; Ma, H.; Sun, Y.; Che, P.; Nie, X.; Wang, T.; Xu, J. Understanding and Measurement for the Binding Energy of Hydrogen Bonds of Biomass-Derived Hydroxyl Compounds. *J. Phys. Chem. A* **2018**, *122*, 843–848.
- (54) Luo, Y.; Ma, H.; Zhang, S.; Zheng, D.; Che, P.; Liu, X.; Zhang, M.; Gao, J.; Xu, J. Binding Energy as Driving Force for Controllable Reconstruction of Hydrogen Bonds With Molecular Scissors. *J. Am. Chem. Soc.* **2020**, *142*, 6085–6092.
- (55) Lei, H.; Wang, Z.; Yang, F.; Huang, X.; Liu, J.; Liang, Y.; Xie, J.; Javed, M. S.; Lu, X.; Tan, S.; Mai, W. NiFe nanoparticles embedded N-doped carbon nanotubes as high-efficient electrocatalysts for wearable solid-state Zn-air batteries. *Nano Energy* **2020**, *68*, 104293.
- (56) Liu, S.; Wang, M.; Sun, X.; Xu, N.; Liu, J.; Wang, Y.; Qian, T.; Yan, C. Facilitated Oxygen Chemisorption in Heteroatom-Doped Carbon for Improved Oxygen Reaction Activity in All-Solid-State Zinc-Air Batteries. *Adv. Mater.* **2017**, *30*, 1704898.
- (57) Yuan, K.; Lützenkirchen-Hecht, D.; Li, L.; Shuai, L.; Li, Y.; Cao, R.; Qiu, M.; Zhuang, X.; Leung, M. K. H.; Chen, Y.; Scherf, U. Boosting Oxygen Reduction of Single Iron Active Sites via Geometric and Electronic Engineering: Nitrogen and Phosphorus Dual Coordination. *J. Am. Chem. Soc.* **2020**, *142*, 2404–2412.